

Electrochemical and *In Situ* Neutron Diffraction Investigations of La-Ni-Al-H Alloys

W. Peng,^a L. Redey,* A. N. Jansen,* D. R. Vissers,* and K. M. Myles

Argonne National Laboratory, Electrochemical Technology Program, Argonne, Illinois 60439, USA

J. M. Carpenter, J. W. Richardson, Jr., and G. L. Burr

Argonne National Laboratory, Intense Pulsed Neutron Source, Argonne, Illinois 60439, USA

J. R. Selman*

Department of Chemical Engineering, Illinois Institute of Technology, Chicago, Illinois 60616, USA

ABSTRACT

The performance of selected $\text{LaNi}_{5-y}\text{Al}_y$ hydride electrodes was studied by extensive electrochemical measurements and *in situ* neutron-diffraction measurements of the deuterated electrode (MD_x) during electrochemical charge-discharge cycles. A small addition of aluminum increased the capacity tenfold under ambient conditions. Increased cell impedance and reduced capacity were noted through the cycle life of $\text{LaNi}_{5-y}\text{Al}_y\text{H}_x/\text{NiO}(\text{OH})$ cells and were found to be associated with the corrosion and leaching of aluminum from the alloy. A high aluminum content alloy ($y = 0.6$), however, compensated for the corrosion loss of aluminum by achieving a longer cycle life than that of a low-aluminum-content alloy ($y = 0.12$). *In situ* neutron diffraction indicated that only alpha phase was present in the low-aluminum-content alloy, $\text{LaNi}_{4.88}\text{Al}_{0.12}\text{D}_{1.1}$, while both alpha and beta phases were present in $\text{LaNi}_{4.4}\text{Al}_{0.6}\text{D}_{1.8}$, the fully charged state. With *in situ* neutron-diffraction measurements, the absolute values of x in the MD_x formula can be determined for various charge/discharge states, while the coulometry of cell cycling measures only the change in x .

Introduction

The nickel/metal hydride (Ni/MH) battery is a strong contender to replace the nickel/cadmium battery because of its superior performance, low impedance, and absence of toxic cadmium.¹⁻³ However, the present Ni/MH battery is limited by hydrogen management problems associated with charge-discharge operation and self-discharge of the battery,⁴ deterioration behavior,⁵ and long-term capacity loss due to corrosion of the MH electrode.⁶ Rare earth metal-based alloys, such as LaNi_5 , preferably with the partial substitution of lanthanum or nickel by a small amount of other metal elements such as Sn, Mn, Co, and Al, seem to be promising alloy materials that improve the performance of the MH electrodes.⁷⁻¹¹ However, the role of alloying components is not yet clearly understood. Therefore, we devised a combination of electrochemical and neutron-diffraction techniques to investigate metal hydrides. This coupling of investigative techniques provides a unique tool for studying the properties of the alloy electrodes *in situ* with respect to composition, atomic structure, and phase change.¹²⁻¹⁶

None of the previous structure studies of LaNi_5D_x and $\text{LaNi}_{5-y}\text{Al}_y\text{D}_x$, which included refinement of deuterium site occupations, has been carried out using operating electrochemical cells. Time-of-flight neutron powder diffraction has been used in connection with a working electrochemical cell, but these studies^{13,14} simply compared data sets to observe the appearance and disappearance of the alpha and beta phases. Several studies used Rietveld profile refinement of time-of-flight neutron-powder-diffraction data for structure studies to determine deuterium site occupations in LaNi_5D_x and $\text{LaNi}_{5-y}\text{Al}_y\text{D}_x$. However, in these studies,^{16,17} the deuterium was inserted into the host by cycled absorption-desorption of deuterium gas. The deuteride was maintained in the cell for neutron-powder-diffraction data sets by an equilibrium overpressure of deuterium gas. Our work presented here yielded comprehensive information on the chemistry of a working electrochemical cell.

In this work, several aluminum substituted LaNi_5 alloys were investigated with respect to their specific capacity, cycling stability, and area specific impedance (ASI). A detailed description of the ASI technique is given in Ref. 18. Correlation of the capacity loss and impedance increase of the cell with dissolution (corrosion) of the metal-hydride alloy component was evaluated throughout the cycle life. *In situ* neutron-diffraction measurements of completely deuterated cells¹⁹ were performed to characterize the electrochemically induced phase transformation and structure change during charge and discharge of the metal hydride electrodes. A special cell was designed, and a deuteration technique was developed to minimize the background scattering to facilitate Rietveld profile refinements of *in situ* neutron-diffraction patterns. The emphasis here is on the cell design, which permits low background investigation and performance comparison between electrochemical and neutron-diffraction measurements on operating cells. A detailed description of the neutron-diffraction methodology and crystallographic details is given elsewhere.²⁰

Experimental

Electrochemical experiments.—The nickel/metal hydride cell reaction can be represented by the following simple cell reaction

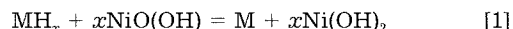


Figure 1 shows the three-electrode cell in which the electrochemical testing was carried out. Hydrogen pressure was not applied to the cell during its operation. The cell consisted of a commercial $\text{NiO}(\text{OH})/\text{Ni}(\text{OH})_2$ positive electrode, a Hg/HgO reference electrode with electrolyte bridge and Luggin capillary, a metal-hydride electrode, and 15 weight percent (w/o) KOH electrolyte. A Teflon mesh separator was used between the working and the counterelectrodes. To ensure uniform current density, we used plane-parallel or jelly-roll electrode combinations to investigate the electrochemical performance of the MH electrode. The alloy powder (Rhône-Poulenc, 36 μm diam) was mixed with 50 mg carbon (Shawinigan Black) per 1 g alloy as a conducting additive and 0.5 ml of DuPont Teflon 30 suspension per 1 g alloy, then pressed onto an expanded nickel mesh to form 1 mm thick electrodes.

* Electrochemical Society Active Member.

^a Dr. Peng is under contract with the Illinois Institute of Technology to perform research at Argonne National Laboratory in the Electrochemical Technology Program.

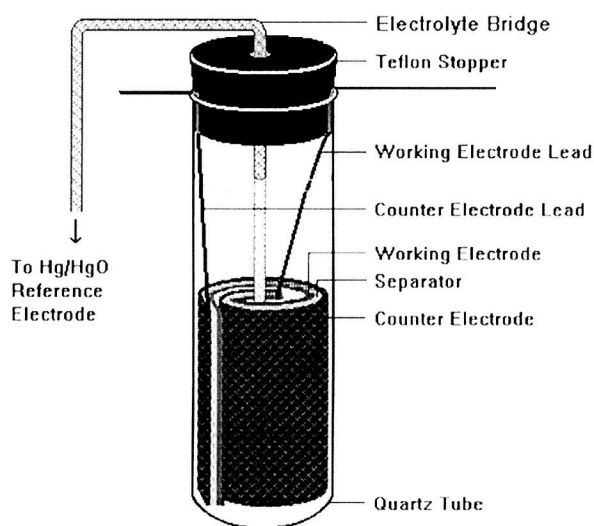


Fig. 1. Schematic diagram of a three-electrode cell used for electrochemical investigations.

We investigated the following alloys: LaNi_5 , $\text{LaNi}_{4.88}\text{Al}_{0.12}$, and $\text{LaNi}_{4.4}\text{Al}_{0.6}$. X-ray examination confirmed that the compound was single phase. The electrochemical properties of the MH electrodes and Ni/MH cells (such as capacity, cell and electrode potential, area specific impedance, and cycle life) were determined by interrupted galvanostatic cycling. The cells cycled between a charge cutoff voltage of 1.47 V and a discharge cutoff voltage of 0.8 V. To clarify the degradation mechanism of $\text{LaNi}_{5-y}\text{Al}_y\text{D}_x$ electrodes and quantitatively assess the dissolution rate of the dissolved alloy components, we applied the inductively coupled plasma-atomic-emission spectrometry (ICP-AES) method to analyze electrolytic solutions taken from the cells during cycling. These data provided the quantitative analysis of the corrosion components. Scanning electron microscopy (SEM) and energy-dispersive x-ray (EDX) analysis provided characterization of the surface morphology of the MH electrode before and after cycling.

A preliminary study aimed at optimizing the MH electrodes was carried out using a criterion of lowering the cell's ASI to the value comparable to that of commercial MH cells. Figure 2 shows the capacity of the three alloys investigated for electrochemical cycling. The LaNi_5 electrode had low, but very stable, capacity. The $\text{LaNi}_{4.4}\text{Al}_{0.6}$ electrode had the highest capacity and exhibited only a relatively small capacity drop. The alloy with the low concentration of aluminum, $\text{LaNi}_{4.88}\text{Al}_{0.12}$, however, had rather poor stability, as indicated by a large capacity decay. The area-specific impedance of these cells was examined by a 30 s current interrupt technique ($\text{ASI}_{30\text{s}}$). These initial cells had an impedance of about $12 \Omega \text{ cm}^2$, as compared to a commercial hydride cell (under similar test conditions), which had an $\text{ASI}_{30\text{s}}$ of $5 \Omega \text{ cm}^2$. Relaxation of the electrode potentials against the reference electrode during interrupt indicated that most of the cell impedance can be attributed to the MH electrode. The contents of MH electrode components, such as Teflon, active carbon, graphite, and aluminum, were varied to fabricate different electrodes, which were subjected to the $\text{ASI}_{30\text{s}}$ measurement. The results reveal that the Teflon content significantly affects the electrode impedance. Figure 3 shows plots of the cell impedance *vs.* discharge capacity (Δx , defined below) for three $\text{LaNi}_{4.4}\text{Al}_{0.6}$ electrodes with Teflon content varying from 0.5 to 2 ml/g alloy. The cell impedance decreased with reduction of the Teflon concentration in the working electrode. Electrodes fabricated with 0.5 ml Teflon/g alloy had a very low cell impedance, $\text{ASI}_{30\text{s}} = 4 \Omega \text{ cm}^2$. This impedance is comparable to the $\text{ASI}_{30\text{s}}$ of a commercial metal hydride AA size cell according to our measurements.

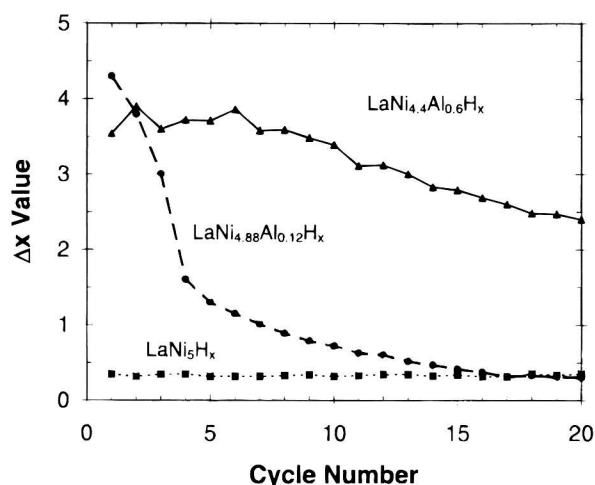


Fig. 2. Cycling behavior of the La-Ni-Al-H alloys for three composition. Fabrication condition of the electrodes was Teflon/alloy = 1.25 ml/g.

Neutron diffraction experiments.—*Cell design for in situ measurements.*—We developed a different cell design for the *in situ* neutron-diffraction measurements to minimize the background due to cell-construction materials, electrolyte, and the presence of remaining protons. Figure 4 shows the cell, constructed in a quartz tube, used in the *in situ* neutron-diffraction measurements. This cell has two main features: (i) the cell used exclusively deuterated components



and (ii) the neutron beam passed through only the lower part of the cell, containing exclusively the metal-deuteride electrode and a minimized amount of electrolyte. However, this cell had a higher impedance than the electrochemical cell in Fig. 1 due to its relatively poor current distribution. To compensate for the high impedance, we discharged the cell to a lower open-circuit potential of 0.6 V.

Construction materials of the *in situ* cell were selected according to chemical compatibility requirements of the cell and the requirements of the neutron-diffraction experiment. The neutronic criteria for selecting materials aimed to reduce interference from the background with the characteristic peaks of metal hydride by (i) avoiding materials containing hydrogen atoms, (ii) minimizing the illuminated mass of container and electrolyte in relation to the electrode material, and (iii) using noncrystalline (non-Bragg-scattering) materials. We conducted a base line measurement of each cell component to determine the background effect on the neutron-diffraction patterns. In

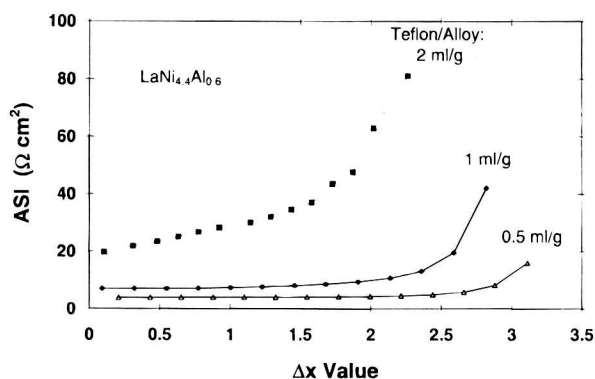


Fig. 3. Plots of the 30 s area-specific impedance ($\text{ASI}_{30\text{s}}$) *vs.* capacity for $\text{LaNi}_{4.4}\text{Al}_{0.6}\text{H}_x$ electrodes with different Teflon loading.

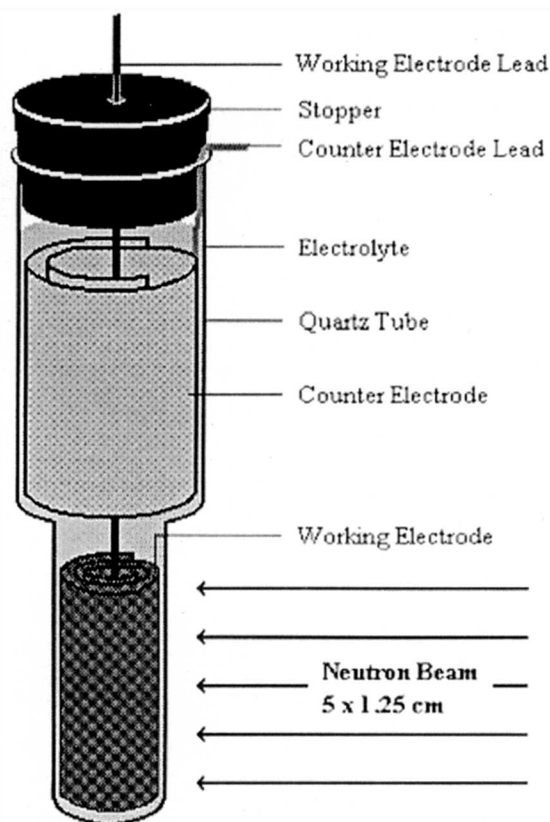


Fig. 4. Schematic diagram of the electrochemical cell for *in situ* neutron-diffraction measurements.

consideration of simplicity, Latroche *et al.*^{13,14} used electrolytic decomposition of D₂O on nickel wire as the positive electrode. We used a fully deuterated NiOOH/Ni(OH)₂ cathode in which the reversible cell reaction



eliminates the gas evolution and electrolyte consumption. However, for the neutron diffraction measurements, it was necessary to exchange the hydrogen atoms contained in the commercial cathode.

Diffraction data collection.—Neutron-diffraction measurements on LaNi_{5-y}Al_yD_x alloys were conducted with the General Purpose Powder Diffractometer (GPPD) at the Intense Pulsed Neutron Source (IPNS) located at Argonne National Laboratory-East. The electrochemical cell consisted of a rolled electrode (4 g LaNi_{5-y}Al_y) in the neutron beam, with a NiO(OD) counterelectrode positioned outside of the beam, both in a 15% KOD/D₂O electrolytic solution. A quartz tube covered with a silicone rubber stopper (Fig. 4) contained the cell. A dry nitrogen purge outside of the quartz tube prevented proton isotope exchange in the cell from the ambient atmosphere. We recorded the neutron-diffraction patterns every 1 h for 30 min simultaneously with electrochemical data.

Neutron powder diffraction (NPD) data were collected as follows: prolonged (6 to 8 h) data sets were accumulated prior to charging, in the fully charged state, and after the subsequent discharge of the LaNi_{4.4}Al_{0.6}D_x electrochemical cell. During the continuous charge and discharge cycles, 30 min data sets were accumulated. For neutron-powder diffraction refinements of the continuous charge and discharge data, three successive data sets were summed. Results from the Rietveld refinements of the fully charged and discharged data are reported below. Details of deuterium concentration and phase composition changes during charging and discharging are reported separately.²⁰

Neutron-diffraction data from these operating cells comprise scattering from five components: the LaNi_{5-y}Al_yD_x electrode, the nickel mesh support, the electrolyte, the Teflon, and the quartz tube. Using a background modeling feature of the generalized crystal structure analysis system (GSAS),²¹ scattering from the electrolyte and quartz tube can be modeled as background, leaving the crystalline nickel, Teflon, and LaNi_{5-y}Al_yD_x phases to consider. Rietveld profile refinements were carried out to obtain precise data corresponding to phase identification, deuterium and metal atom siting, and phase composition as a function of charge-discharge state.

Deuteration of NiO(OD) electrode and determination of H/D ratio.—Two identical pieces of NiO(OH) electrodes (removed from Ni/Cd cells) were cycled in 15% KOD/D₂O solution 16 to 20 times to produce deuterated NiO(OD) electrodes. We exchanged and analyzed the electrolyte after every four cycles to determine the remaining hydrogen content of the overall cell. For accurate refinement of the neutron diffraction data, a H/D ratio of less than 0.02 is required. In order to verify the fully deuterated condition of the cell for the *in situ* neutron diffraction measurement, we developed an infrared (IR) technique to monitor the H/D ratio during the deuteration process. Three standard samples, 10% KOD/D₂O (no H), 5% H₂O/14% KOD/81% D₂O, and 10% KOH/H₂O (no D), were tested by middle range Fourier transform infrared (FTIR) (wavenumbers 500 to 4000 cm⁻¹) in a BaF₂ cell in order to establish a calibration diagram.

Figure 5 shows the FTIR spectra of the pure solutions. The characteristic absorption peaks of KOD/D₂O appeared as sharp peaks at 2650, 2500, and 1200 cm⁻¹ (top, Fig. 5), while those of KOH/H₂O are at 3300 (broad) and 1650 (narrow) cm⁻¹ (bottom, Fig. 5). The intensity of the -OH stretching peak at 3300 cm⁻¹ was reduced fourfold when the water concentration changed from 100% to 5% (middle, Fig. 5). The absorption peaks of hydrogen and deuterium are separated, allowing an estimation of H/D ratios once absorbance-concentration calibrations are made. With this technique we examined four samples successively taken from the cell during the deuteration process. Figure 6 shows the FTIR spectra of deuterated solutions. The hydrogen characteristic peak at 3300 cm⁻¹ from the first to the last (4th) sample decreased in sequence, from around 5% to approximately 0%, indicating the effectiveness of the deuteration technique. Neutron-diffraction experiments confirmed this observation. There was no heavy background scattering present in the neutron-diffraction patterns.

Results and Discussion

***In situ* neutron diffraction measurements and Rietveld profile refinements of the neutron-diffraction data of operating electrochemical cells were successfully performed. The structure-refinement data, analyzed along with the electrochemical evaluation, provide insight into the relationship between structural and electrochemical phenomena of the metal hydride cells.**

Capacity comparison.—The discharge capacity is indicated by the change in the value of *x* in the formula LaNi_{5-y}Al_yH_x. However, the absolute value of *x* at the end of discharge cannot be easily determined electrochemically. In our work we define Δ*x* as the amount of hydrogen (deuterium) released from the hydride alloy upon electrochemical discharge and designate it to represent the cell capacity. The electrochemically measured value of Δ*x*_E is based on the coulometry. That is

$$\Delta x_E = \frac{3600}{eN_A} Q_M \frac{M}{W_a} = \frac{Q_M M}{26.8 W_a} \quad [3]$$

where *Q*_M is the measured discharge capacity (Ah), *e* is the electron charge (C), *N*_A is Avogadro's number, *M* is the formula weight of the alloy (g/mol), and *W*_a is the mass of the alloy (g).

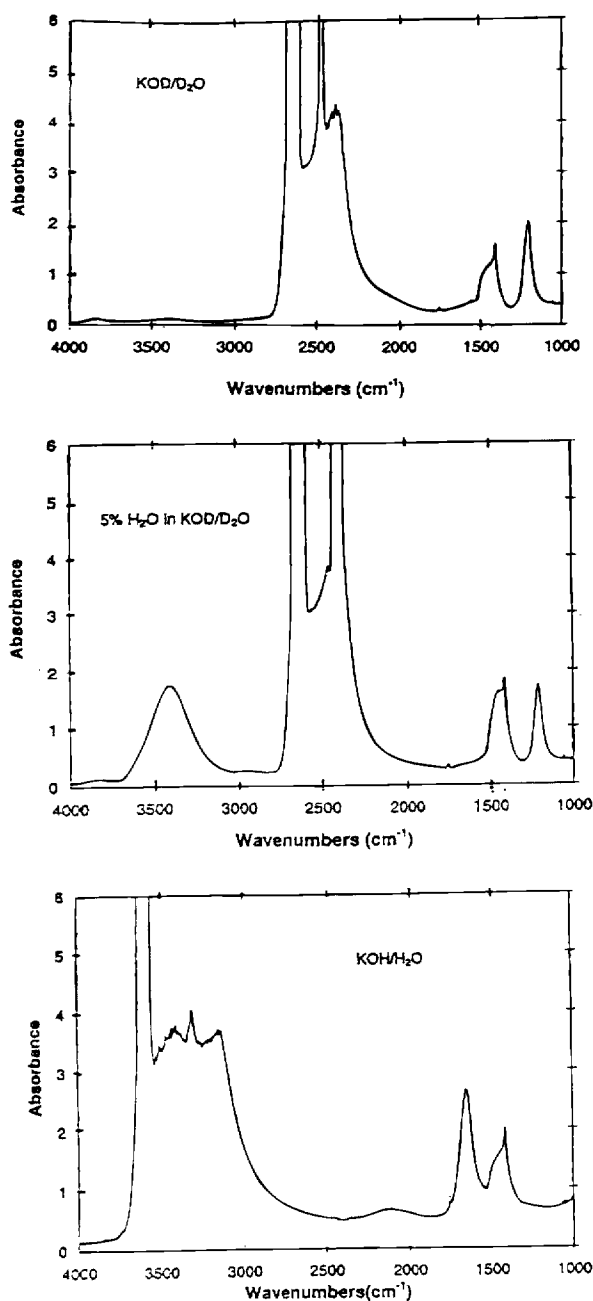


Fig. 5. FTIR spectra of standard solutions.

One advantage of neutron-diffraction analysis over the coulometric calculation is that it can provide an absolute value of x . Thus, the discharge capacity observed by neutron diffraction, Δx_N , is the difference between the absolute x values at full charge (x_c) and discharge (x_d). That is

$$\Delta x_N = x_c - x_d \quad [4]$$

Figure 7 shows plots of cell potential *vs.* capacity for different La-Ni-Al-H alloys at the same discharge current and cutoff voltage. Data were obtained from the electrochemical cell shown in Fig. 1 but without use of a reference electrode. The cell potential changes from a fully charged state, where Δx_E is zero, to a fully discharged state, where Δx_E reaches its maximum at the discharge cutoff voltage. As shown in Fig. 7, there are distinct differences in the capacities of the MH electrodes (dischargeable in the same cell potential range). The LaNi₅ hydride exhibited low specific capacity, while the aluminum-substituted alloys have dramatically increased cell capacity up to more than 10 times higher than that of the pure

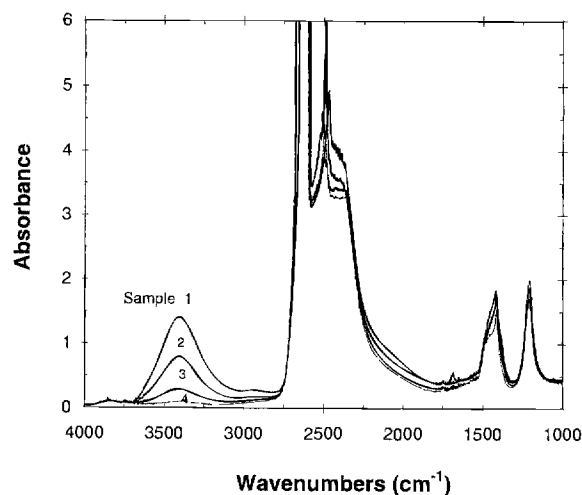


Fig. 6. FTIR spectra of deuterated solutions.

LaNi₅ parent alloy in the same voltage range between the upper and lower cutoff voltage. The effect of higher aluminum concentrations on the capacity improvement can be partly explained by the lowered hydrogen equilibrium pressure, P_{eqH_2} , which is the plateau pressure on pressure-composition isotherms obtained from solid/gas measurement (see Fig. 8). The LaNi₅ alloy has an absorption P_{eqH_2} of about 1.83 atm,⁴ while the LaNi_{5-y}Al_y alloys have an absorption P_{eqH_2} of about 0.11 atm for $y = 0.5$ ⁴ and about 0.8 atm for $y = 0.2$.²²

The open-circuit electrode potential of a hydride electrode, ϵ , corresponds to a_{H_2} , the activity (pressure) of hydrogen gas on the electrode surface which is equilibrated with atomic hydrogen in a hydride electrode.⁹ For our 15% KOH electrolyte at 25°C, this can be expressed as²³

$$\epsilon \text{ (vs. HgO/Hg)} = -0.928 - 0.030 \log(a_{H_2}) \quad [5]$$

where a_{H_2} is the activity of hydrogen in atmospheres. In an ambient electrochemical cell in which the cell pressure, P , is about 1 atm, alloy electrodes with an a_{H_2} value of $P_{eqH_2} < a_{H_2} \leq P$ (at the end of charge) would generate larger discharge capacity. Figure 9 shows plots of open-circuit electrode potentials, measured at the end of the 30 s current interrupt, for three alloy compositions during the discharge process. The LaNi₅H_{Δx=0} electrode exhibits a less negative potential, while the LaNi_{4.4}Al_{0.6}H_{Δx=0} electrode is more negative. The potential of the fully charged alloy decreases toward more negative values as the aluminum content (y) in LaNi_{5-y}Al_y increases. The hydrogen activities of these alloy electrodes in the charged state, estimated by Eq. 5, are 0.5 atm for LaNi₅, 0.8 atm for LaNi_{4.88}Al_{0.12}, and 1.1 atm for LaNi_{4.4}Al_{0.6}. For LaNi₅, $a_{H_2} < P_{eqH_2}$ results in a lowered cell capacity (below the plateau value). For LaNi_{4.88}Al_{0.12} and LaNi_{4.4}Al_{0.6}, however, $a_{H_2} > P_{eqH_2}$, which results in an increase in the capacity to its plateau value. Because the cell is not pressurized, a_{H_2} cannot exceed 1 atm, which is the reason for the low utilization of LaNi₅ in our system. The addition of aluminum does not increase the theoretical capacity, or number of hydrogen/deuterium sites, but merely enhances the thermodynamics to favor hydride formation over hydrogen gas evolution. This is evident by a lowering of the hydrogen absorption equilibrium plateau as depicted in Fig. 8.

Table I shows the results of the *in situ* neutron-diffraction measurements of x and Δx for the three alloys in their fully charged and fully discharged states. Figure 10 shows changes of Δx from electrochemical data, x from neutron diffraction experiments, and open-circuit cell potential as a function of time upon discharge for LaNi_{4.4}Al_{0.6}D_x electrode. The discharge capacity given by neutron-diffraction (Δx_N) is in good agreement with that (Δx_E) calculated by coulometry of the galvanostatic cycling. Note, however,

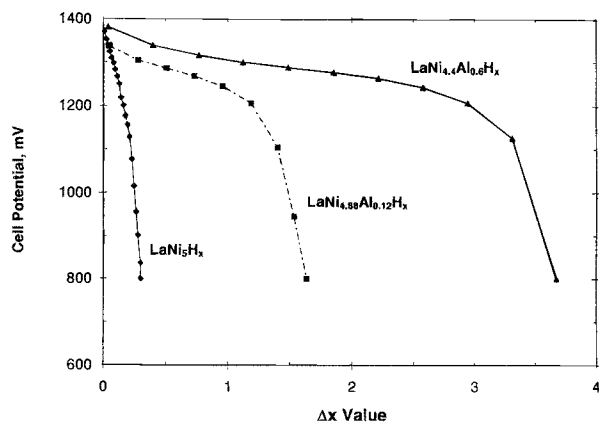


Fig. 7. Closed-circuit potential for $MH_x/NiO(OH)$ cells as function of discharge capacity.

the x value at the fully discharged point is not zero, suggesting that deuterium is not completely depleted from the deuterated alloy when the alloy is electrochemically discharged to the discharge cutoff voltage. In this case, Δx_E from coulometry is different from the x value at any given time during discharge. At this time, the residual uncertainty in the data is too large to correlate Δx_E and x quantitatively, although the general shape is in good agreement.

Structural information.—Rietveld profile refinements of the neutron powder diffraction data from operating electrochemical cells were successful. Figure 11 shows the profile fit for fully charged $LaNi_{4.4}Al_{0.6}D_{1.8}$ in the d -spacing range 0.75 to 2.8 Å, which illustrates the effective modeling of the mixed-phase structures of $\alpha-LaNi_{4.4}Al_{0.6}D_{1.3}$, $\beta-LaNi_{4.4}Al_{0.6}D_{3.6}$, and Ni mesh. Apparent in this figure is the very minor contribution (recognized as an oscillatory component in the observed and calculated patterns) from the quartz tube and electrolyte. Only with these contributions kept very small are we able to study these structures, in such detail, *in situ*. Comparable fits were obtained for $LaNi_5$ powder, $LaNi_5D_x$ electrodes, and $LaNi_{4.4}Al_{0.6}$ powder.

Crystallographic model.—The crystal chemistry of substituted $LaNi_5$ deuterides has been thoroughly studied using

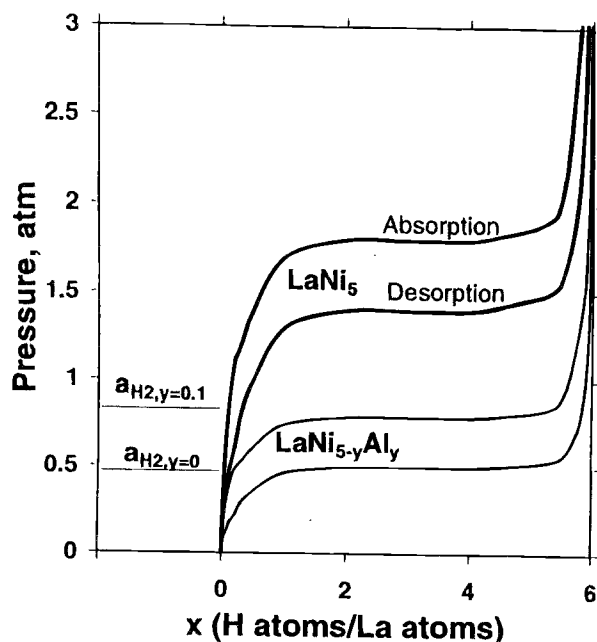


Fig. 8. Qualitative pressure-composition isotherms for $LaNi_5$ and $LaNi_{5-y}Al_y$ metal hydrides at room temperature.

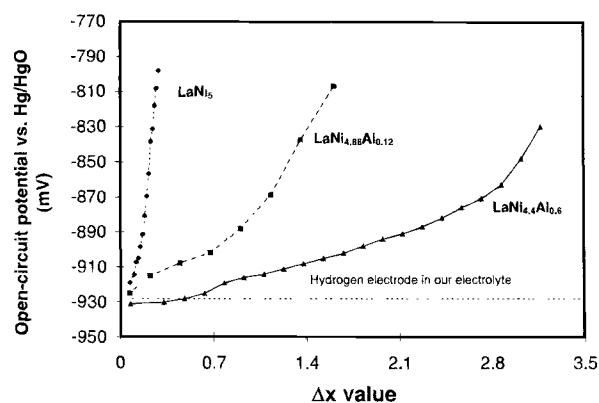


Fig. 9. Open-circuit potential for $MH_x/NiO(OH)$ cells as function of discharge capacity.

neutron diffraction,^{13,24-27} although never, to our knowledge in an operational electrochemical cell. The works of Percheron-Guegan *et al.*,²⁴ Soubeyroux *et al.*,²⁶ and Latroche *et al.*¹³ are particularly relevant to this work. In brief, these materials are derivatives of $LaNi_5$ ($CaCu_5$ structure-type; hexagonal space group $P6/mmm$; illustrated in Fig. 12) containing two crystallographically distinct nickel sites, Ni(1) and Ni(2), as shown. It has been found²⁴ that many $LaNi_5$ alloys are deficient in La, resulting in the introduction of two additional nickel sites: (a) Ni(3), pairs of which replace a single La atom, and (b) Ni(4), which replaces (three at a time) Ni(1) and is displaced from Ni(1) sites toward vacated La sites. In aluminum-substituted $LaNi_5$, Al substitutes selectively on Ni(2) sites. Deuterides of $LaNi_5$ (and its substituted forms) cover a range of deuterium concentrations (x) from 0.1 to 6.7 per La atom. In the range $x < \sim 1.0$, the α -phase is the preferred phase, while above this level, the β -phase forms. Under some conditions, both phases will co-exist.¹³ Percheron-Guegan *et al.*²⁴ presented a model involving five deuterium sites for $LaNi_5D_x$ and its derivatives. These sites represent interstitial locations which, under the proper conditions, are large enough for deuterium. Table II shows the fractional coordinates for all metals (including La depletion) and deuterium atoms in this five-atom model. For most deuterides, only some of these deuterium sites are occupied. Soubeyroux *et al.*²⁶ found that, in the α -phase, D atoms are preferentially located on 12n sites (identified as D(4) in Table II). Deuterium site occupancies in the β -phase are strongly dependent upon the type(s) and amount(s) of metal(s) substituting for Ni. This five-atom, La-depletion model was used as a starting point for our refinements of alloy powders and *in situ* electrodes during charge/discharge cycling of electrochemical cells.

In the process of modeling the anisotropic peak broadening observed in substituted alloys, we found that we could get an improved refinement when introducing an additional degree of freedom to the lattice-parameter refinements. This we accomplished using space group $Cmmm$, an orthorhombic sub-group of $P6/mmm$. In $Cmmm$, the b and c axes remain the same, and the new a axis is taken as a face diagonal in the original $P6/mmm$ cell, with approximate length $3a$. Site multiplicities and identifiers for La, Ni, etc., are changed according to the new space group

Table I. Values of Δx and x values for the fully charged and discharged states in La-Ni- D_x alloys with and without aluminum.

Deuterated alloy	Fully charged x	Fully discharged x	Δx_N	Δx_E
$LaNi_5D_x$	0.8(2)	0.5(2)	0.30	0.28
$LaNi_{4.88}Al_{0.12}D_x$	1.1(2)	0.4(4)	0.68	0.66
$LaNi_{4.4}Al_{0.6}D_x$	1.8(4)	0.71(8)	1.12	1.15

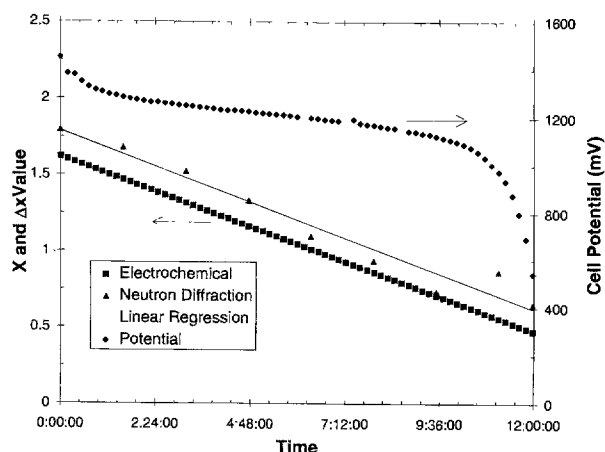


Fig. 10. Plots of x , Δx , and cell potential vs. running time of the *in situ* neutron diffraction measurement for $\text{LaNi}_{4.4}\text{Al}_{0.6}\text{D}_x$.

symmetry. Furthermore, Ni(2) nickel sites, shared by Ni and Al, are split into two distinct sites: Ni(2a), a 4f site, and Ni(2b), a 2c site. Refinements in space group Cmmm suggested that the Al atoms are preferentially sited on the 2c sites. While this discovery is interesting and potentially important to our eventual understanding of the role of substitutional metals in LaNi_5 , the improvements to the Rietveld fits were marginal. It was concluded that this was an appropriate subject area for future studies, but was not fundamentally important to the primary objective of this work: identifying and quantifying deuterium concentration changes during electrochemical charge/discharge cycling. Even though preferential deuterium siting is probable, if preferential Al siting exists, refinement in P6/mmm should accurately model overall changes. Further discussion of this possible orthorhombic ordering will be given in another report.²⁰

Rietveld refinement results.—Our refinement of LaNi_5 powder indicated very slight La depletion ($\delta = 0.003$). As

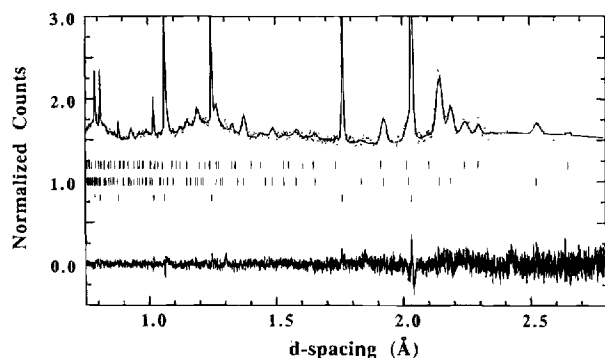


Fig. 11. Rietveld profile plot for $\text{LaNi}_{4.4}\text{Al}_{0.6}\text{D}_{1.8}$, which is composed of ~80% $\alpha\text{-LaNi}_{4.4}\text{Al}_{0.6}\text{D}_{1.3}$ and ~20% $\beta\text{-LaNi}_{4.4}\text{Al}_{0.6}\text{D}_{3.6}$. Data points correspond to observed neutron counts (normalized to the incident spectrum, but no background subtracted), the solid curve superimposed on the observed data corresponds to the calculated intensities from the three-phase refinement, while the lower curve is the difference between observed and calculated intensities (on the same scale). Vertical bars represent the positions for nonextinct reflections in the respective phases: Ni mesh, bottom row; α -phase, middle row; β -phase, top row. Since the scale is chosen to amplify the contributions from the α - and β -phases, some Ni mesh peaks extend beyond the graph. Recognizable in the observed and difference patterns (e.g., $d = 2.42, 1.85, 1.30 \text{ \AA}$) are peaks from Teflon, which was used as a spacer in the electrode assembly. We were unable to identify the structure of this phase.

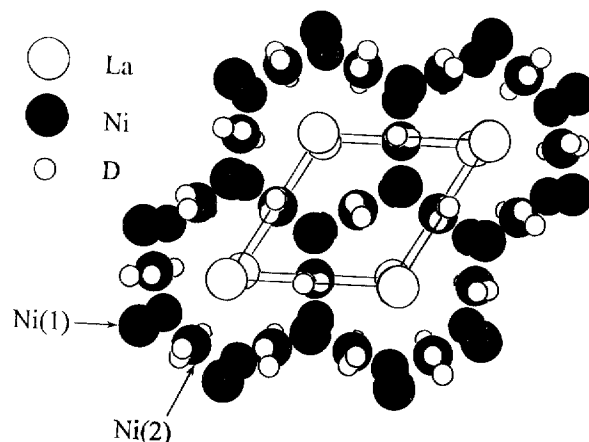


Fig. 12. Hexagonal representation of LaNi_5D_x .

noted in previous work,^{24,28,29} the diffraction peaks exhibited peak broadening, indicating some degree of microstrain. Bragg peaks were roughly twice the width for a typical unstrained material in all crystallographic directions. Calculated deuterium concentrations for the LaNi_5 electrode in its fully charged and fully discharged states were 0.8(2) and 0.5(2), respectively (see Table III). Peak breadths were 10 to 20 times the strain-free value. Unfortunately, there were no long runs corresponding to the fully charged and fully discharged states, and thus the values reported are from 30 min of data collection. Nonetheless, these values are roughly as expected, with a change in deuterium concentration (Δx) of 0.3, in excellent agreement with the electrochemically determined value (0.3).

Peak breadths for the $\text{LaNi}_{4.4}\text{Al}_{0.6}$ powder were comparable to those of the LaNi_5 powder (2 to 3 times strain-free), while those for the corresponding electrodes were dramatically broader than observed in LaNi_5 , ranging from 60 to 400 times the strain-free value. This extreme broadening is handled effectively (see Fig. 11) in the Rietveld refinement using a peak-shape function²¹ which allows the modeling of crystallographic direction-dependent broadening. We found that the broadening was greatest for axial (001) reflections, and nearly identical for the α -phase in the charged and discharged electrodes. Broadening in basal plane, (hk0) reflections, was greatest for the fully charged α -phase. Interestingly, the basal plane broadening for fully discharged α -phase and the minority β -phase in the fully charged cell was the same, even though the axial broadening was twice as large in the β -phase.

Refined structural parameters for $\text{LaNi}_{4.4}\text{Al}_{0.6}$ powder, and for fully charged and discharged cells, are given in

Table II. Fractional coordinates used as the base line for refinements of alloys and electrodes.

Atom	Site	x	y	z	n
La	1a	0	0	0	1-8
Ni(1)	2c	1/3	1/3	0	2-38
Ni(2)	3g	1/2	0	1/2	3-y
Al(2)	3g	1/2	0	1/2	y
Ni(3)	6i	0.287	0.574	0	38
Ni(4)	2e	0	0	0.313	8
D(1)	3f	1/2	0	0	0
D(2)	4h	1/3	1/3	0.369	0
D(3)	6m	0.136	0.272	1/2	0 ^a
D(4)	12n	0.455	0	0.117	x ^b
D(5)	12o	0.204	0.408	0.345	0

^a D(3) occupancy nonzero only in the β -phase of charged $\text{LaNi}_{4.4}\text{Al}_{0.6}\text{D}_x$.

^b Each charge state for both LaNi_5 and $\text{LaNi}_{4.4}\text{Al}_{0.6}\text{D}_x$ has its own D(4) occupancy.

Table III. Refined structural parameters for alloys and their deuterides.

Nominal composition	LaNi ₅	LaNi ₅ D _{0.8}	LaNi ₅ D _{0.5}	LaNi _{4.4} Al _{0.6}	LaNi _{4.4} Al _{0.6} D _{1.8}	LaNi _{4.4} Al _{0.6} D _{0.7}
<i>a</i> (Å) α-phase	5.0203(1)	5.0188(4)	5.0158(5)	5.0398(1)	5.0501(6)	5.0462(3)
<i>c</i> (Å) α-phase	3.9793(1)	3.9764(6)	3.9756(6)	4.0248(1)	4.0448(10)	4.0473(7)
vol. fract. (%)	100.0	100.0	100.0	100.0	78.2	100.0
δ	0.003(2)	0.003	0.003	0.001(1)	0.028(1)	0.026(7)
<i>n</i> _{Al(2)}	—	—	—	0.60(2)	0.36(9)	0.63(6)
<i>X</i> _{D(4)}	—	0.455(24)	0.489(95)	—	0.434(6)	0.429(7)
<i>Z</i> _{D(4)}	—	0.170(17)	0.109(27)	—	0.151(8)	0.160(9)
<i>n</i> _{D(4)}	—	0.8(2)	0.5(2)	—	1.30(10)	0.71(8)
<i>a</i> (Å) β-phase	—	—	—	—	5.2999(19)	—
<i>c</i> (Å) β-phase	—	—	—	—	4.2048(64)	—
vol. fract. (%)	0.0	0.0	0.0	0.0	21.8	0.0
<i>n</i> _{Al(2)}	—	—	—	—	0.60 ^a	—
<i>n</i> _{D(3)}	—	—	—	—	1.6(5)	—
<i>n</i> _{D(4)}	—	—	—	—	2.0(4)	—
Total deuterium	—	0.8(2)	0.5(2)	—	1.8(4)	0.71(8)
<i>R</i> _p	6.04	4.32	5.97	4.03	1.84	1.62

^a Fixed according to the nominal Al composition.

Table III. These data confirm earlier reports^{13,24,25} of lattice-parameter changes and deuterium siting in electrochemically charged cells. Fully charged LaNi_{4.4}Al_{0.6}D_x is ~80 volume percent (v/o) α-LaNi_{4.4}Al_{0.6}D_{1.3} and 20 v/o β-LaNi_{4.4}Al_{0.6}D_{3.6}, with an overall deuterium site, referred to as D(4) in Table II, was occupied in the α-phase. The β-phase, on the other hand, showed measurable occupancy on both the 6m and 12n [D(3) and D(4)] sites, in agreement with earlier work.²⁴ During the continuous *in situ* discharging, the volume fraction of β-phase decreased progressively, eventually giving way to pure α-phase. In the fully discharged state only α-LaNi_{4.4}Al_{0.6}D_{0.7} is present, *i.e.*, overall deuterium concentration $x = 0.7$ D. This corresponds to a concentration change $\Delta x = 1.1$, again exactly as measured electrochemically.

The deuterium concentration from Rietveld calculations of the continuous discharge cycle in Fig. 11 were determined by refining the scale factors of the alpha LaNi_{4.4}Al_{0.6}D_x phase and the beta LaNi_{4.4}Al_{0.6}D_x phase. All NPD parameters of the alpha phase were allowed to refine, whereas the β-phase parameters were kept at the values determined in the fully charged study as shown in Table II and Table III.

In situ measurements of operating electrodes always show scattering contributions from the quartz container and KOD electrolyte. Any effort to assign background intensities qualitatively due to these amorphous materials are doomed to failure because they inevitably remove Bragg scattering erroneously. Instead, our Rietveld profile-refinement model includes a background function designed to fit the scattering from the amorphous materials. This function is a truncated sine series, closely related to the correlation function used to describe amorphous materials, with terms corresponding to the scattering amplitudes and interatomic spacing of characteristic pairs of atoms in the material. The quartz (amorphous SiO₂) tube, for instance, has a short-range structure made up of SiO₄ tetrahedra, joined along corners and edges to form a continuous network. Characteristic interatomic distances are Si-O 1.61, O-O 2.63, Si-Si 2.97 Å, etc. Within the Rietveld refinement, the amplitudes and spacing are adjustable parameters. It has been shown³⁰ that an approach such as this does effectively decouple crystalline and noncrystalline scattering, thus allowing access to crystallographic details. All refinements in electrochemical cells were carried out using this background function.

Corrosion analysis.—Figure 13 shows the plots of discharge capacity (Δx) of LaNi_{4.4}Al_{0.6} and LaNi_{4.88}Al_{0.12} vs. their cycle number. Both cells have an average impedance of ASI_{30s} = 5 Ω cm². Compared with the performance of the cells in Fig. 2 which have a higher ASI_{30s} of 12 Ω cm² (due to a higher Teflon content in the alloy electrodes), the low-

impedance cells exhibit a reduced capacity loss per cycle and, consequently, an improved cycle life. However, the trend of the curves in Fig. 13 (low impedance) remained similar to that in Fig. 2 (high impedance). Figure 14 shows the change of the cell impedance vs. the cycle number of the LaNi_{4.4}Al_{0.6} electrode. There is a plateau for each cycle from the fully charged state to the fully discharged state, at the end of which the impedance sharply increases. The length of the ASI plateau decreased throughout the cycle life. One possible reason for this behavior is the selective dissolution of the aluminum component. The ICP-AES analysis of the electrolytic solutions from these cells quantitatively indicated dissolved aluminum in the cell electrolyte throughout the cycle life.

Two cells were made with 0.5 g LaNi_{4.88}Al_{0.12} and 0.5 g LaNi_{4.4}Al_{0.6}, respectively. Originally, the LaNi_{4.88}Al_{0.12} electrode contained 3.77 mg aluminum, the LaNi_{4.4}Al_{0.6} electrode contained 19.51 mg aluminum, and both cells contained about 100 ml electrolyte. Electrolyte samples were collected during cycling and submitted for ICP-AES analysis, results of which are shown in Fig. 15. The dissolved aluminum from the LaNi_{4.88}Al_{0.12} electrode into the electrolyte was 5 μg/ml after 12 cycles, and 14 μg/ml after 29 cycles. The 14 μg/ml is equivalent to 37% of the original aluminum content of the electrode. The higher concentration of aluminum in the LaNi_{4.4}Al_{0.6} alloy, however, can compensate for the corrosion loss of aluminum for a longer time than in the case of the LaNi_{4.88}Al_{0.12} alloy. Figure 15 indicates that the rate of aluminum dissolution of LaNi_{4.4}Al_{0.6} is relatively low. After 160 cycles the dissolved aluminum was 16 μg/ml; that is to say, about 8% of the aluminum originally in the alloy leached out. Figure 16

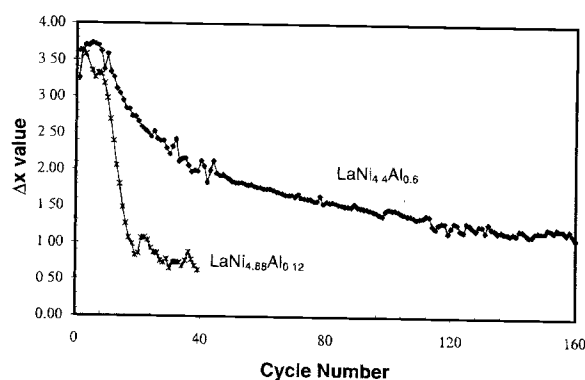


Fig. 13. Comparison of cycling behavior of the LaNi_{4.88}Al_{0.12}H_x and LaNi_{4.4}Al_{0.6}H_x cells. The fabrication condition of the electrodes was Teflon/alloy = 0.5 ml/g.

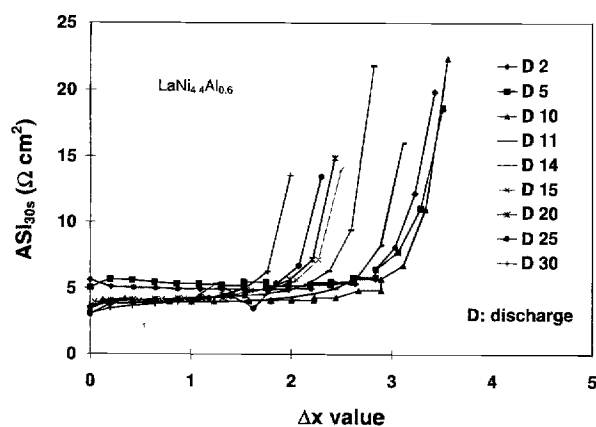


Fig. 14. Impedance of the $\text{LaNi}_{4.4}\text{Al}_{0.6}\text{H}_x$ cell as functions of discharge capacity through thirty cycles.

shows the same data converted into atomic ratio of aluminum (y) in the alloys and plotted *vs.* cycle number. As expected, lanthanum and nickel were not detectable (<0.1 g/ml) in the electrolyte of either cell (no soluble species at this pH).

Our experimental results of the electrode potential and *in situ* neutron diffraction support the observation that the higher aluminum-content alloy exhibits greater resistance to corrosion. An electrode working in the more negative-potential region impedes corrosion. Open-circuit electrode potentials ϵ (*vs.* Hg/HgO reference) of the MH electrodes were measured at each end of the 30 s current interrupt during cycling. Table IV gives ϵ values obtained for three alloys in their fully charged, halfway discharged, and fully discharged states. The open-circuit potential of LaNi_5 decreases toward more negative values on the addition of aluminum; *i.e.*, the $\text{LaNi}_{4.4}\text{Al}_{0.6}$ electrode exhibits a more negative potential than that of $\text{LaNi}_{4.88}\text{Al}_{0.12}$ and LaNi_5 .

It is possible that an electrode working partly in the beta domain is helpful in terms of resistance to corrosion, as was suggested in Ref. 6. Refinement of deuterium occupancy in a $\text{LaNi}_{5-y}\text{Al}_y$ electrode indicates that the alpha phase in $\text{LaNi}_{4.88}\text{Al}_{0.12}\text{D}_x$ can accept more deuterium ($x = 1.1$) than the alpha phase for LaNi_5D_x ($x = 0.8$). In contrast, however, both alpha and beta phases were found to be present in the material of $\text{LaNi}_{4.4}\text{Al}_{0.6}\text{D}_x$ at its fully charged state. This is indicative of the aluminum contributing additional stability to deuterium in the sites.

Figure 17 shows the scanning electron micrographs of the $\text{LaNi}_{4.4}\text{Al}_{0.6}$ before cycling (a) and after 160 cycles (b). For the noncycled electrode, there were jagged alloy parti-

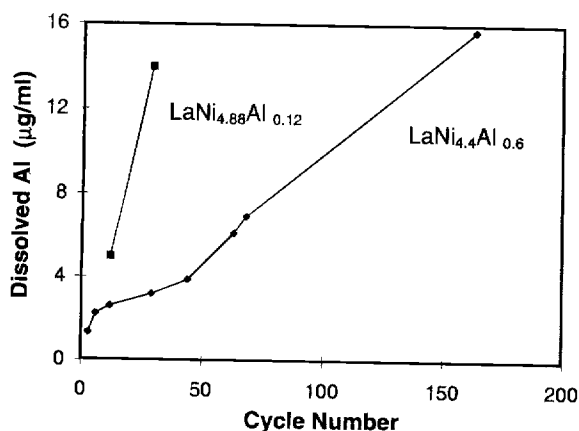


Fig. 15. Dissolved aluminum in electrolyte through the cycle life of the $\text{LaNi}_{5-y}\text{Al}_x$ electrode.

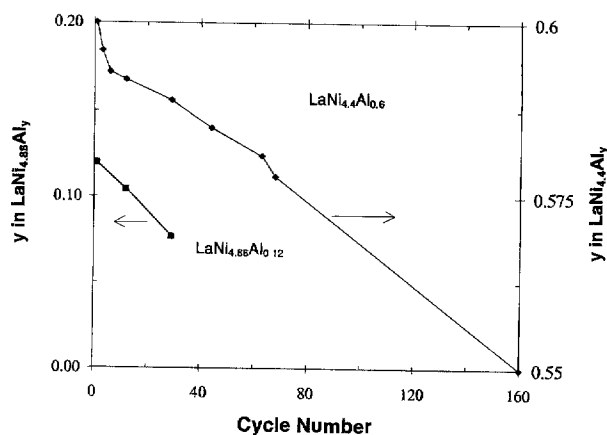


Fig. 16. Change of the aluminum content (y) in the $\text{LaNi}_{5-y}\text{Al}_x$ alloys during cell cycling.

cles with sharp edges and relatively large, irregular grains. The particles broke into smaller pieces after the electrode was subjected to cycling, and became rounded and cracked. The EDX analysis indicated a lower atom fraction of aluminum on the cycled alloy particles. This result is consistent with that of the ICP-AES analysis of the electrolyte from the cycled cell, which shows that aluminum is leaching from the alloy electrode into the electrolyte during cycling. Surface modification of the alloy particles or introduction of other corrosion-suppressing alloying elements^{31,32} is necessary to achieve longer cycle life for practical applications.

Summary

We have designed and developed a cell to conduct *in situ* investigations simultaneously of both the electrochemical and the structural (neutron-diffraction) characteristics of $\text{LaNi}_{5-y}\text{Al}_y\text{D}_x$ metal hydride electrodes. With the addition of aluminum, the utilization of the theoretical capacity of LaNi_5 was enhanced at ambient conditions (1 atm) by a lowering of the hydrogen-absorption equilibrium plateau. The Rietveld crystallographic-structure analysis provided the location of both aluminum and deuterium in the lattice. The extra deuterium in $\text{LaNi}_{5-y}\text{Al}_y\text{D}_x$ appears to be entering the alpha-phase for the alloy with low aluminum addition ($y = 0.12$), but to be forming both alpha and beta phases for the alloy with higher aluminum addition ($y = 0.6$).

Neutron-diffraction measurements of the metal hydride (MH_x) correlate quite well with the electrochemical measurements of Δx . The capacity fade of the aluminum-containing alloy is associated with the corrosion of aluminum in the alloy. Neutron diffraction can be a powerful tool in conjunction with *in situ* electrochemical cell operation to understand better how alloying constituents affect the electrochemical properties of electrode materials.

Acknowledgment

The authors thank Rhone-Poulenc for supplying the metal hydride alloys and Todd Bofinger for his assistance in assembling the cells. This research was sponsored by the U.S. Army Research Office, Research Triangle Park, NC, through the ARO Fuel Cell/Battery Research Hub at the Illinois Institute of Technology. The research was conducted at Argonne National Laboratory-East, which is operat-

Table IV. Open-circuit potentials of La-Ni-D electrodes with and without aluminum.

Deuterated alloy	Fully charged potential (mV)	Half-discharged potential (mV)	Fully discharged potential (mV)
LaNi_5D_x	-919	-863	-788
$\text{LaNi}_{4.88}\text{Al}_{0.12}\text{D}_x$	-925	-895	-807
$\text{LaNi}_{4.4}\text{Al}_{0.6}\text{D}_x$	-930	-904	-830

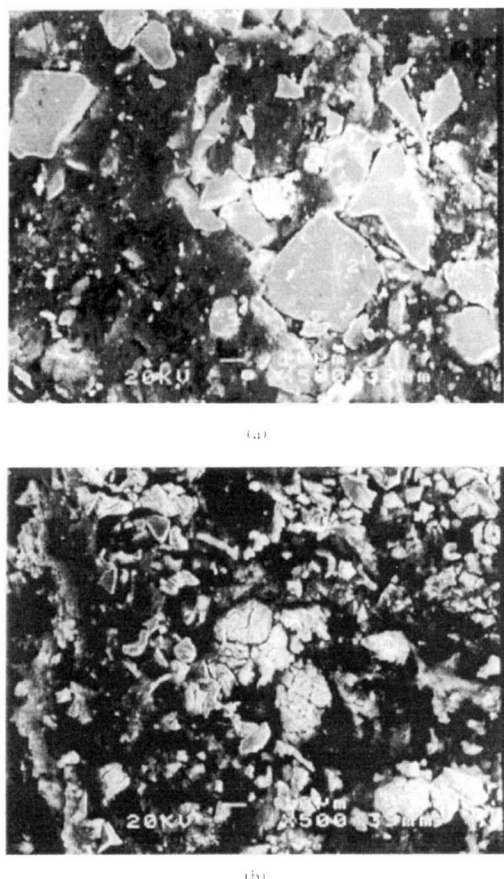


Fig. 17. Scanning electron micrographs of an $\text{LaNi}_{4.4}\text{Al}_{0.6}$ electrode (a) before cycling and (b) after 160 charge-discharge cycles

ed by the University of Chicago for the U.S. Department of Energy under Contract No. W-31-109-Eng-38.

Manuscript submitted Nov. 18, 1996; revised manuscript received May 23, 1997.

Argonne National Laboratory assisted in meeting the publication costs of this article.

REFERENCES

1. S. R. Ovshinsky, M. A. Fetcenko, and J. Ross, *Science*, **260**, 176 (1993).
2. M. Ikoma, S. Hamada, N. Morishita, Y. Hoshina, H. Matsuda, K. Ohta, and T. Kimura, in *Hydrogen and Metal Hydride Batteries*, P. D. Bennett and T. Sakai, Editors, PV 94-27, p. 370, The Electrochemical Society Proceedings Series, Pennington, NJ (1994).
3. N. Furukawa, *J. Power Sources*, **51**, 45 (1994).
4. C. Iwakura, Y. Kajiya, H. Yoneyama, T. Sakai, K. Oguro, and H. Ishikawa, *This Journal*, **136**, 1351 (1989).
5. N. Kuriyama, T. Sakai, H. Miyamura, I. Uehara, H. Ishikawa, and T. Iwasaki, *J. Alloys Compd.*, **202**, 183 (1993).
6. A. Percheron-Guegan, M. Latroche, J. C. Achard, Y. Chabre, and J. Bouet, in *Hydrogen and Metal Hydride Batteries*, P. D. Bennett and T. Sakai, Editors, PV 94-27, p. 196, The Electrochemical Society Proceedings Series, Pennington, NJ (1994).
7. B. V. Ratnakumar, C. Witham, B. Fultz, and G. Halpert, *This Journal*, **141**, L89 (1994).
8. S. Mukerjee, J. McBreen, J. J. Reilly, J. R. Johnson, G. Adzic, K. Petrov, M. P. S. Kumar, W. Zhang, and S. Srinivasan, *ibid.*, **142**, 2278 (1995).
9. A. Anani, A. Visintin, S. Srinivasan, A. J. Appleby, J. J. Reilly, and J. R. Johnson, in *Hydrogen Storage Materials, Batteries, and Electrochemistry*, D. A. Corrigan and S. Srinivasan, Editors, PV 92-5, p. 105, The Electrochemical Society Proceedings Series, Pennington, NJ (1992).
10. T. Sakai, K. Oguro, H. Miyamura, N. Kuriyama, A. Kato, H. Ishikawa, and C. Iwakura, *J. Less-Common Met.*, **161**, 193 (1990).
11. J. S. Cantrell, T. A. Beiter, and R. C. Bowman, Jr., *J. Alloys Compd.*, **207/208**, 373 (1994).
12. L. Redey, K. M. Myles, F. J. Rotella, J. W. Richardson, G. P. Felcher, R. L. Hitterman, and R. Kleb, in *Hydrogen Storage Materials, Batteries, and Electrochemistry*, D. A. Corrigan and S. Srinivasan, Editors, PV 92-5, p. 258, The Electrochemical Society Proceedings Series, Pennington, NJ (1992).
13. M. Latroche, A. Percheron-Guegan, Y. Chabre, C. Poinssignon, and J. Pannetier, *J. Alloys Compd.*, **189**, 59 (1992).
14. M. Latroche, J. Rodriguez-Carvajal, A. Percheron-Guegan, and F. Bouree-Vigneron, *ibid.*, **218**, 64 (1995).
15. C. Poinssignon, N. Dalphraise, M. Latroche, J. Pannetier, and A. Percheron, *MRS Proc.*, **293**, 401 (1993).
16. E. H. Kisi, E. Mac A. Gray, and S. J. Kennedy, *J. Alloys Compd.*, **216**, 123 (1994).
17. E. M. A. Gray and E. H. Kisi, in *Neutron Scattering Hydrogen Materials*, A. Furrer, Editor, p. 110, World Scientific, Singapore, Singapore (1994).
18. L. Redey and D. R. Vissers, *This Journal*, **130**, 231 (1983).
19. W. Peng, L. Redey, D. R. Vissers, K. M. Myles, J. Carpenter, J. Richardson, and G. Burr, Abstract 64, p. 81, The Electrochemical Society Meeting Abstracts, Vol. 96-1, Los Angeles, CA, May 5-10, 1996.
20. G. L. Burr, W. Peng, T. Bofinger, L. Redey, A. N. Jansen, J. C. Carpenter, and J. W. Richardson, Jr., *J. Less-Common Met.*, Submitted.
21. A. C. Larson and R. B. Von Dreele, Generalized Crystal Structure Analysis System, Los Alamos National Laboratory, LAUR 86-748 (1986).
22. E. D. Snijder, G. F. Versteeg, and W. P. M. van Swaaij, *J. Chem. Eng. Data.*, **39**, 405 (1994).
23. D. Berndt, *Maintenance-Free Batteries*, p. 75, Research Studies Press, Ltd., Taunton, Somerset, England (1993).
24. A. Percheron-Guegan, C. Lartigue, J. C. Achard, P. Germi, and F. Tasset, *J. Less-Common Met.*, **74**, 1 (1980).
25. A. Percheron-Guegan, C. Lartigue, and J. C. Achard, *ibid.*, **109**, 287 (1985).
26. J. L. Soubeyroux, A. Percheron-Guegan, and J. C. Achard, *ibid.*, **129**, 181 (1987).
27. H. Hayakawa, K. Nomura, Y. Ishido, E. Akiba, S. Shin, H. Asano, F. Izumi, and N. Watanabe, *ibid.*, **143**, 315 (1988).
28. P. Thompson, J. J. Reilly, and J. M. Hastings, *ibid.*, **129**, 105 (1987).
29. C. Lartigue, A. LeBail, and A. Percheron-Guegan, *ibid.*, **129**, 65 (1987).
30. J. W. Richardson, Jr. and J. Faber, *Advanced X-Ray Analysis*, C. S. Barrett, J. B. Cohen, J. Faber, Jr., R. Jenkins, D. E. Leyden, J. C. Russ, and P. K. Predecki, Editors, p. 143, Plenum Press, New York (1986).
31. T. Sakai, A. Yuasa, H. Ishikawa, H. Miyamura, and N. Kuriyama, *J. Less-Common Met.*, **172-174**, 1194 (1991).
32. T. Ikeya, K. Kumai, and T. Iwahori, *This Journal*, **140**, 3082 (1993).